

# FABRICATION AND MEASUREMENTS OF PLASTIC SCINTILLATING FIBERS

Ph. Rebourgeard, F. Rondeaux, J.P. Baton, G. Besnard, H. Blumenfeld,  
M. Bourdinaud, J. Calvet, J.C.Cavan, R. Chipaux, A. Giganon, J. Heitzmann,  
C. Jeanney, P. Micolon, M.Neveu, T. Pedrol, D. Pierrepont.

*CEA Saclay,  
Direction des Sciences de la Matière,  
Département d'Astrophysique, de physique des Particules, de physique Nucléaire et de  
l'Instrumentation Associée,  
91191 Gif-sur-Yvette Cedex, France.*

---

## Abstract

60 km of plastic scintillating fibers, 1 mm in diameter, have been manufactured using a preform/tube technology. The fibers consist of a polystyrene core surrounded by a polymethylmethacrylate cladding. The fabrication method is described and evaluated both qualitatively and quantitatively. A great effort has been made in order to measure the optical properties of the polymer at the different steps of the production. The global process efficiency is not more than 40 % due to the yield of the polymerization process. Using a ternary blue scintillator, the mean light yield for a minimum ionizing particle in a 1 mm diameter fiber at a distance of 1 meter is  $5.4 \pm 0.6$  photoelectrons. The mean attenuation length fitted between 0.5 m and 2.0 m is  $1.9 \pm 0.2$  m. Some specific experiments that give independent measurements of core and interface losses are also reported. The principal cause of light loss is due to the lack of transparency of the polystyrene which leads to a spectral shift in fiber emission. This absorption already appears in the preform rods indicating that the purification and the polymerization process are of great importance. The attenuation length related to core losses is measured at the level of 3 m. The interface losses are about  $10^{-5}$ - $10^{-4}$  per reflection leading to an equivalent attenuation length of 7m.

---

## 1. Introduction

Saclay has been one of the pioneer laboratories in the field of plastic scintillating fibers and during more than 10 years we have carried on with a R&D program on the fabrication and the characterization of plastic luminescent fibers.

Since the mid 80th's scintillating fibers have grown to be a commercial product. Many companies in Japan, US, Italy and France can provide plastic luminescent fibers which have satisfactory optical properties and which are manufactured in an industrial environment. This leads to a competitive cost and a good quality control. In the same period, the potential applications of scintillating fibers have appeared more clearly. The relative poor radiation hardness (around 10 kGy) and the problems related to light readout of small fibers in a reduced space and in a high magnetic field (even if impressive progress has been made) have limited the use of plastic scintillating fibers in HEP experiments. In particular,

scintillating fibers are not suitable for the LHC tracking environment and both CMS and ATLAS collaborations [33-34] have preferred silicon or gaseous strip detectors for this purpose. On the other hand, scintillating fibers have found applications in other experiments where irradiation is less critical, as in CHORUS [35], and are to be used with VLPC readout in the D0 upgrade [36]. Some detectors have also been proposed for radiobiology or astrophysics, and many other applications remain to be found. Low dose applications will probably not require further technological developments since both polystyrene/polymethylmethacrylate and polystyrene/fluorinate cladding technologies are today mature.

These evolutions addressed directly the question of the continuation of our R&D program. In order to take the right decision we have engaged a systematic evaluation of our fabrication method and of loss factors. The tests had to measure the yield of our PS/PMMA technology and to evaluate the technological and financial effort that could lead to significant improvements in fiber properties. The main scientific results of this study are reported in this paper.

In the first section we present the theory of plastic scintillating fibers. After a brief history, we focus on the scintillator composition and on the propagation of rays in the presence of core attenuation and of interface losses. A simple phenomenological model is developed and related to physical losses.

The second part is devoted to the tests of our technology. We describe with some details the fabrication method and we present the measurements of preforms and derived fibers. This gives many informations about the quality and the reproducibility of the process.

Finally, in the third part, we return with light propagation and present more specific measurements on cladding, core and interface light losses. These measurements give experimental arguments to the model developed in the first section. They explain the deviation from pure exponential attenuation in term of spectral shift of the fiber emission. The transparency of polystyrene preform and of fiber core are compared in order to evaluate the damage related to the drawing process. Interface losses are also studied with a new simple setup which reproduces the effective operating conditions of scintillating fibers.

## **2. Plastic scintillating fibers**

### **2.1 A brief history of fiber technology**

Plastic scintillating fibers in their actual form were proposed in the early eighties by S.R. Borenstein [1] who used polyvinyltoluene (PVT) as core material. The basic idea is simple and consists in the drawing of a polymer scintillator surrounded by a different polymer which has a lower refractive index in order to obtain an optical light pipe. The practical realization of this concept was not trivial since a good fiber requires a high transparency of both core and cladding materials and a high quality interface at the junction of the two polymers.

Rapidly, a Saclay group proposed to replace PVT by polystyrene and the first fibers were manufactured in 1983 [2-4]. They were drawn from 40 mm diameter preforms consisting of PS rods clad with polyvinyl acetate (PVA). The optical index of these polymers is given in table 1. PS was doped with bPBD and dPOPOP [see table 2] resulting in a ternary scintillator. Polystyrene was chosen as scintillator base because it has a high refractive index and is easier to draw than PVT.

The first fibers presented some drawbacks due to the cladding material. To allow a uniform deposition of the coating, the PS rods, 40 mm in diameter, were partly immersed in a polyvinyl acetate solution over a few mm. After many rotations around their horizontal axis, a thin uniform coating was achieved. A long drying of the preform was found necessary to avoid degassing, microbubble formation and cladding removal during the fiber drawing. An other problem was due to the adherence properties of PVA, since the fibers, kept on storage wheels for a long time, were sticking together even at 20°C. However, these fibers were used successfully for the construction of the UA2 Scintillating Fiber Detector in 1985 [5-6]. The gluing problem was solved with the help of an aluminium sputtering of the PVA cladding which acts as a protection and avoids moreover the cross-talk between two adjacent fibers of the final detector.

The maximal PVA thickness that could be deposited around a 40 mm PS rod was not more than 0.4 mm resulting in a 10  $\mu\text{m}$  cladding around the 1 mm fiber. Since total reflection at the core-cladding interface requires a minimum 1-2  $\mu\text{m}$  cladding layer, this technology limits the minimum achievable fiber diameter to 0.20 mm.

At the mid eighties great interest was shown in high resolution scintillating fibers with diameter in the 50  $\mu\text{m}$ -100  $\mu\text{m}$  range. Many developments were made in Japan, France and CERN on this type of device. It appeared rapidly that both technology and scintillator composition had to be modified in order to solve the problem of cladding thickness and to avoid cross-talk [7-8]. For this purpose, we developed the new PMMA technology described in section 3. As shown in table 2, PMMA has a refractive index greater than PVA resulting in lower N.A. and trapping efficiency. However PS/PMMA fibers offer in other respects many advantages that balance the N.A. reduction.

We produced in 1988-1989 active targets, 40 mm in diameter and 250 mm in length, consisting of small compacted 50  $\mu\text{m}$  microfibers doped with PBBO. They were tested successfully with an Image Intensifier-CCD readout at CERN-PS in 1990 [9-10].

Microfibers based on a PS/PMMA composition have also been manufactured by Kuraray but we have no direct informations on their technology. Different binary scintillator formulations such as PS/3HF or PS/PMP have also been tested by other group in order to solve the problem of cross-talk. Good results have been reported with PMP microfibers [11-13]. Particle tracking with microfibers is a very beautiful technique but until now the limitation in fiber light yield (2 hits/mm @ 0.5 m) and of CCD readout have limited the applications in high energy physics experiments.

More recently, the interest of fiber manufacturers has been focused on the hadronic colliders experiments in the framework of SSC and LHC programs. Many studies have been devoted to both comprehension and improvement of radiation hardness and a technology using fluorinate cladding has been developed [14]. Unfortunately PS based fibers exhibit serious limitations and are not suitable for high radiative environments. It has been proposed to use polysiloxane scintillators [15] in order to overcome this limitation but to our best knowledge no scintillating fiber of this type has been produced.

## 2.2 Scintillators for plastic fibers

Scintillating fibers are used to detect ionizing particles that pass through the core. In polystyrene, a minimum ionizing particle deposits around  $dE / dx = 200 \text{ keV} / \text{mm}$  in the fiber core. This energy must

be converted into photons in a efficient manner and those photons are transmitted through the fiber and detected by a photocathode or by a silicon photodetector.

We have measured with a Perkin Elmer spectrofluorimeter the emission of undoped PS rods [10]. The spectrum is plotted in Fig. 1 for an excitation at 252 nm. The maximum of emission is found at 305 nm, in discrepancy with the emission at 330 nm reported by Berlman [16] on PS solution in cyclohexane but, in good agreement with other results obtained with plastic polystyrene [17-18]. This can be interpreted as a consequence of residual monomer styrene emission. At 305 nm Rayleigh scattering and electronic absorption lead to a very poor PS transparency as can be seen in Fig. 2 [6]. Moreover, it must be noted that pure PS exhibits a very low quantum efficiency  $\eta_x$  which is not more than 3% [16]. As a result pure PS fibers have a poor scintillation.

Both problems find a solution with a binary scintillator composition. The introduction in the polymer base of a primary dopant, designated hereafter by Y, fulfills two different requirements:

i/ It shifts the scintillation emission to a wavelength greater than 305nm, where PS transparency is higher.

ii/ It increases the scintillation efficiency by strong dipole-dipole coupling (Förster's non radiative transfer), between PS and the dopant.

Organic molecules which present a high absorption at 305 nm and a large Stokes' shift (spectral difference between absorption and emission peaks) are generally used with a sufficient concentration in order to increase dipole-dipole coupling. Non radiative Förster's transfers are described by a rate parameter  $k_{XY}$  given by [20-23]

$$k_{XY} \propto \frac{1}{\tau_{0X}} \left[ \frac{R_0}{R} \right]^6 \quad (1)$$

where  $\tau_{0X}$  is the natural fluorescence lifetime of PS, R the mean separation between solute and polymer molecules and  $R_0$  a constant distance proportional to the overlap between PS emission and dopant absorption. The non radiative transfers compete with the normal fluorescence emission of PS and it has been shown [19] that the transfer efficiency between X and Y is correctly approximated by

$$\eta_{XY} = \frac{\eta_x + \sigma[Y]/[Y]_0}{1 + \sigma[Y]/[Y]_0} \quad (2)$$

$\eta_x$  is the quantum efficiency of the polymer base,  $\sigma$  a model dependant parameter equal to 2.05, [Y] the dopant concentration and  $[Y]_0$  a critical concentration related to the distance  $R_0$  by

$$[Y]_0 = 0.396R_0^{-3} \quad (3)$$

where  $R_0$  is expressed in nm and  $[Y]_0$  in mol/l. Eq. (2) predicts an increase of transfer efficiency as a function of dopant concentration.

To illustrate this mechanism we report on measurements performed with a binary (PS+PBBO) scintillator. Plastic rods have been prepared with various dopant concentrations and with rough surfaces in order to avoid light trapping [8, 10]. The samples have been studied with a Perkin Elmer spectrofluorimeter. We have observed the fluorescence emission of PBBO (at 410 nm) as a function of the excitation wavelength and we have measured the ratio between the direct excitation of the dopant (at 332 nm) and the indirect one via polystyrene excitation (at 252 nm). This method leads to very clear results and gives a direct measurement of the transfer efficiency  $\eta_{XY}$ . The results are plotted in Fig. 3 and fitted by Eq. (2). We have found that the critical concentration is  $[Y]_0=10.4$  g/l for PBBO and that the PS quantum efficiency is  $\eta_x=10.1\%$ . We can estimate the critical distance with help of Eq. (3). Using the fitted value of  $[Y]_0$  we find  $R_0=2.4$  nm in good agreement with values already reported for PS+TPB scintillators [18]. The high PS quantum efficiency deduced from Fig. 3 (10% instead of 3% as reported by Beriman) can again be explained by the styrene residual monomer [17]. The quantum efficiency of the scintillator is given by the product of  $\eta_{XY}$  with the dopant efficiency denoted by  $\eta_Y$ . Since Förster's transfer has a very short time constant, this scheme predicts that both scintillation emission and decay time are characteristic of the dopant. The absolute scintillation yield also depends on the primary energy transfer between ionizing particles and PS since the dopant concentration is too low to enable a direct ionization of Y molecules. The primary process, related to the probability of  $\pi$  electrons excitation in PS molecules, has a very low energetic efficiency (less than 7% [19]).

For many primary dopants such as bPBD and p-terphenyl, the scintillation emission is still in a spectral range where PS presents a significant absorption and a second dye denoted by Z must be added in order to shift again the luminescence. The second dopant must present a high quantum efficiency but a high concentration is not required since Förster's transfers are not necessary. In ternary scintillators, the first part of the energy transfer follows the binary scheme but the fluorescence photons emitted by the first dye are absorbed by the second dopant and reemitted at a longer wavelength. In scintillating fibers, the spatial properties of the radiative transfer between Y and Z is of particular interest but was rarely studied in solid samples [24], [8], [10]. Fig. 4 illustrates the radiative transfer in the ternary PS+bPBD+dPOPOP scintillator. Thin doped PS films have been prepared, roughned and measured with a spectrofluorimeter. We observe the progressive shift from bPBD emission to dPOPOP emission as a function of film thickness. The mean transfer length which is also the mean free path of Y photons in the scintillator and is denoted by  $\Lambda_{YZ}$ , can be deduced from the figure [10]. For a dPOPOP concentration  $[Z]$  equal to 0.02% in mass we have found it around 350  $\mu\text{m}$ . Obviously, a transfer length  $\Lambda_{YZ}$  greater than the fiber diameter will cause a decrease of fiber light yield since part of the Y photons are not absorbed in the fiber core and unless they are trapped at the core/cladding or cladding/air interface they will escape resulting in a bad YZ transfer [7]. As a result the value of  $\Lambda_{YZ}$  limits the minimum achievable fiber diameter. Provided that all Y photons are converted inside the fiber, the quantum efficiency of the scintillator is equal to  $\eta_{XY}\eta_Y\eta_Z$ .

Most secondary dopants present a significant overlap between their absorption and emission spectra as shown for dPOPOP in Fig. 5. This leads to the autoabsorption process which lowers the fiber efficiency. Many authors have pointed out that a high dopant concentration must increase autoabsorption [7], [14], [22]. True as a first approximation, the mechanism is somewhat more complex since PS itself presents a significant absorption. The losses induced by the dopant are just an additional cause of absorption and are generally lower than PS losses in the largest part of the fluorescence spectrum. As a result, the dopant concentration can be increased in order to achieve a low transfer length without resulting in a dramatic polymer absorption.

However, the use of ternary scintillators can be avoided by employing molecules such as PBBO, PMP, TPB or 3HF that present an important Stokes' shift as primary dopant. This leads directly to a blue-green scintillator emission but when contemplating bigger shifts it must be noted that green or red dyes have generally a long decay time since Einstein's relations predict a  $\lambda^2$  dependance of life time [16]. Moreover they are not matched with usual photodetectors (Photomultipliers, Image Intensifiers). This is an important drawback for certain applications but cannot be avoided in radiation hard fibers which must overcome the radiation damage of PS in the blue part of the spectrum [14].

Finally the total number of photons emitted by the scintillator can be expressed as

$$n_{\gamma_0} = \frac{dE}{dx} \cdot \frac{1}{E_{\gamma}} \quad (4)$$

where  $E_{\gamma}$  is the energy required for the emission of one scintillation photon.  $E_{\gamma}$  depends inversely on the scintillation efficiency. Values in the range between 100 and 150 eV are typical for a ternary composition. Thus, a 1 mm scintillator excited by a minimum ionizing particle will produce  $n_{\gamma_0} \cong 1500 - 2000$  photons but it will be seen in the next sections that, due to the poor trapping efficiency and to the propagation losses, only a small part of this light can be detected effectively at the end of the fiber.

### 2.3 Light trapping by scintillating fibers

Fluorescent molecules present a dipole emission but are randomly oriented during the polymerization and the fiber drawing. Thus, at the macroscopic level, the scintillator emission is isotropic resulting in a light injection very different from the normal use of optical fibers.

A scintillating fiber is modeled as shown in Fig.6 by a cylindrical core of radius  $\rho$  coated with a thin cladding material of external radius  $\rho_c$ . Three interfaces can be observed in this model: the core-cladding interface which is of particular interest in respect to fiber operation, the cladding-air interface which can also give total reflection since cladding refractive index is higher than air index and the core-air interface at both ends of the fiber where the scintillation photons have to be collected by a photodetector. We denote hereafter by  $n_{co}$  and  $n_{cl}$  the refractive index of core and cladding materials, by  $n_a$  the refractive index of air and by  $n_e$  the refractive index of end coupling that may be air or any other material as an optical grease for instance. From the dispersion relations of PS and PMMA [26] we find  $n_{co}=1.613$  and  $n_{cl}=1.502$  at 450 nm. As a result, the numerical aperture NA is equal to 0.59 ( $\theta_{NA}= 36^\circ$ ) (half angle of emission cone in air) in PS/PMMA fibers.

Plastic scintillating fibers have a large core diameter ranging from 50  $\mu\text{m}$  in microfibers to 2.0 mm in the largest fibers. The modal parameter [25] given by

$$V = \frac{2\pi}{\lambda} \cdot \rho \cdot \sqrt{n_{co}^2 - n_{cl}^2} \quad (5)$$

is high ( $V=8000$  in a 1 mm diameter PS/PMMA fiber at 450 nm) and, as a result, light propagation can be described in the approximation of geometrical optics [25].

A ray trapped by the fiber is fully described by two invariants of the propagation [25]. We will use hereafter the propagation angle  $\theta$  relative to the fiber axis and the closest approach to fiber axis denoted by  $r_{ic}$  which is related to the incidence angle  $\Omega$  relative to the normal  $n$  to the core-cladding interface by

$$(\cos \theta)^2 + \left(\frac{r_{ic}}{\rho} \sin \theta\right)^2 = (\sin \Omega)^2 \quad (6)$$

If the incidence angle  $\Omega$  is greater than the critical incidence angle  $\Omega_c = \sin^{-1}(n_{cl}/n_{co})$ , the ray is trapped at the core-cladding interface. Eq. (6) shows that skew rays defined by  $r_{ic} \neq 0$  can be trapped with propagation angles  $\theta$  larger than the critical one  $\theta_c = \cos^{-1}(n_{cl}/n_{co})$ . These rays emitted outside the N.A. are designated hereafter as tunnelling rays in opposition to bound rays defined by  $\theta \leq \theta_c$  that may be skew or meridional. The trapping condition deduced from Eq. (6) can be rewritten as

$$r_{ic} \geq y_c(\theta) \equiv \rho \sqrt{1 - \left(\frac{\sin \theta_c}{\sin \theta}\right)^2}. \quad (7)$$

We can then find the efficient part of the transverse section relative to ray capture at the core-cladding interface which yields

$$S(\theta) = \pi \rho^2 \left[ 1 - \frac{2}{\pi} \sin^{-1} \left( \frac{y_c(\theta)}{\rho} \right) - \frac{2}{\pi} \frac{y_c(\theta)}{\rho} \sqrt{1 - \left( \frac{y_c(\theta)}{\rho} \right)^2} \right] \quad (8)$$

As long as  $\theta \leq \theta_c$ , we have  $y_c = 0$  and all the fiber cross section is efficient in respect to light trapping at the core-cladding interface and  $S(\theta) = \pi \rho^2$ . As a result the fiber efficiency relative to bound rays is given by

$$\varepsilon_{br} = \frac{1}{2} (1 - \cos \theta_c) = \frac{1}{2} \left( 1 - \frac{n_{cl}}{n_{co}} \right). \quad (9)$$

which is also the trivial estimation of fiber efficiency in the meridional approximation.

For tunneling rays, the situation is somewhat more complex since part of the section gives refracted rays. The contribution to the trapping efficiency in respect to core-cladding interface can be expressed as

$$\varepsilon_{tr} = \frac{1}{4\pi} \int_{\theta_c}^{\theta_i} \frac{S(\theta)}{\pi \rho^2} 2\pi \sin \theta d\theta \quad (10)$$

The above integral is limited to the critical angle  $\theta_c = \sin^{-1}(n_e/n_{co})$  relative to the core-coupling interface at fiber end.

Eq. (10) gives the contribution of tunneling rays to fiber efficiency and can be calculated analytically [10]. If the optical coupling is perfect  $n_e = n_{co}$ , the global trapping efficiency  $\epsilon_{trap}$  relative to the core-cladding interface is given by

$$\epsilon_{trap} = \epsilon_{br} + \epsilon_{tr} = \frac{1}{2} \left[ 1 - \left( \frac{n_{cl}}{n_{co}} \right)^2 \right] \quad (11)$$

which yields 6.64% (9.0%) in a PS/PMMA (PS/PVA) fiber. This value can be compared to the classical estimation given by Eq. (9) that yields only 3.44% (4.7%). As a result, it can be seen that about 50% of the trapped rays have propagation angle larger than the critical one. Now, if we consider the effect of coupling, Eq. (10) yields  $\epsilon_{trap} = 5.2\%$  for an exit in air ( $n_e=1.0$ ) and  $\epsilon_{trap} = 6.2\%$  for an exit in an optical grease ( $n_e=1.5$ ) [27].

On the other hand, if the incidence angle  $\Omega$  is less than the critical incidence angle  $\Omega_c$ , the ray can leave the core and is refracted in the cladding according to Snell's law. Depending on the angle of incidence at the cladding-air interface, the ray will either leave the fiber or be reflected on the external interface and refracted again in the fiber core. In this case, it must be noted that the invariants do not allow a further trapping by the core-cladding interface and the ray will continue to travel part in the core, part in the cladding until it is lost or it exits by one end of the fiber. These rays are designated hereafter as cladding rays and many studies have shown that due to the poor quality of cladding-air interface, they vanish after a few tens of cm in a 1mm fiber [29]. As a result, they are negligible except in very short fibers. We will also present in section 4 a direct evidence of this assertion.

#### 2.4 Light propagation in scintillating fibers

A ray emitted at a distance  $z$  to fiber end and trapped at the core-cladding interface fulfills Eq. (7) and follows a total path

$$L(z, \theta) = \frac{z}{\cos(\theta)} \quad (12)$$

in fiber core. From simple geometrical considerations, it can be seen that the number of reflections at the core-cladding interface is given by

$$n(z, \theta, r_{ic}) = \frac{z \tan \theta}{2\rho} \left[ 1 - \left( \frac{r_{ic}}{\rho} \right)^2 \right]^{-1/2} \quad (13)$$

Denoting by  $n_\gamma$  the total amount of photons emitted in  $4\pi$  and by  $\xi(\lambda)$  the normalized spectral distribution, the photons trapped at the core cladding interface in the spectral range between  $\lambda$  and  $\lambda + d\lambda$  and in the angular range between  $\theta$  and  $\theta+d\theta$  are given by



$$dn_{trapped} = n_{\gamma 0} \xi(\lambda) \frac{S(\theta)}{\pi \rho^2} \sin \theta d\theta d\lambda \quad (14)$$

Before they reach fiber end, some photons will be lost. The first cause of attenuation is from the lack of transparency of core material (diffusion or absorption) and is described at a particular wavelength  $\lambda$  by the photon mean free path  $\Lambda_{core}(\lambda)$ . An other cause of attenuation is related to interface losses and is usually described by the discrepancy  $\varepsilon$  with respect to total reflection. It depends on the incidence angle  $\Omega$  at the core cladding interface and on the wavelength  $\lambda$  [28], [30-31]. As a result, the attenuation of the scintillation emission over a distance  $z$  is given by

$$\alpha(z, \lambda, \theta, r_{ic}) = e^{-\frac{1}{\cos \theta \Lambda_{core}(\lambda)} z + \ln[1 - \varepsilon(\Omega, \lambda)] \frac{z \tan \theta}{2\rho \sqrt{1 - (r_{ic}/\rho)^2}}} \quad (15)$$

At the fiber end, the remaining photons are refracted in the coupling material or reflected back in the fiber core depending on the propagation angle. We denote by  $\rho_F(\theta, \lambda)$  the Fresnel's losses and by  $\eta(\theta, \lambda)$  the photodetector efficiency for a particular wavelength and angle. If  $\theta \leq \theta_e$ , we can express the amount of photoelectrons as

$$dn_{pe}(z, \theta, \lambda) = \frac{1}{2} n_{\gamma 0} [1 - \rho_F(\theta, \lambda)] \eta(\theta, \lambda) \xi(\lambda) \sin \theta d\theta d\lambda \quad (16)$$

$$\times \int_{y_c(\theta)}^{\rho} \frac{4\sqrt{\rho^2 - y^2}}{\pi \rho^2} \alpha(\lambda, \theta, y, z) dy$$

where the efficient surface  $S(\theta)$  has been replaced by an equivalent integration over the  $y$  coordinates of emission point.

Eq. (16) gives the exact yield of a scintillating fiber but is difficult to handle analytically and requires further simplification:

i) We first assume that the fiber emission spectrum does not depend on the fiber length. This hypothesis will be discussed in section 4 and is valid for a fiber length greater than 0.5m. As a result, the  $\lambda$  dependance in Eq. (16) can be replaced by the value of the various quantities at the mean emission wavelength  $\bar{\lambda}$ .

ii) for the tunneling rays emitted outside N.A. ( $36^\circ$  in air for a PS/PMMA fiber), the efficient fraction of fiber section is reduced according to Eq. (8). Moreover, tunnelling rays undergo much more reflections than bound rays and, for a standard air coupling, they are refracted at large angle at the end of the fiber. Furthermore, the photodetector efficiency decreases rapidly at large incidence. Thus, we have many arguments to limit the analysis to the numerical aperture of the fiber. This assumption will be checked in section 4 and leads to an error smaller than 15% for a fiber length greater than  $z=1$  m.

iii) Over the angular range defined by the above assumption ( $-36^\circ$  to  $36^\circ$ ) the variation of photodetector efficiency is generally small and the Fresnel's losses are close to the normal incidence expression given by

$$\rho_F = \left( \frac{n_{co} - n_e}{n_{co} + n_e} \right)^2 \quad (17)$$

Since  $y_c(\theta) = 0$  for bound rays, substituting  $y = \rho \sin u$  into Eq. (16) and assuming that  $\varepsilon$  is small and verifies  $\ln(1 - \varepsilon) \cong -\varepsilon$ , Eq. (16) can be rewritten as:

$$\begin{aligned} dn_{\gamma_e} = & n_{\gamma_0} \eta(\bar{\lambda}) [1 - \rho_F] \sin \theta d\theta \cdot e^{-\frac{z}{\Lambda_{core}(\bar{\lambda}) \cos \theta}} \\ & \times \frac{2}{\pi} \int_0^{\pi/2} e^{-\frac{z}{2\rho} \frac{\varepsilon(\Omega, \bar{\lambda}) \tan \theta}{\cos u}} \cos^2 u du \end{aligned} \quad (18)$$

It can be shown from Eq. (6) that at small propagation angle the mean incidence  $\Omega$  varies linearly with  $\theta$  and does not depend very much on  $r_{ic}$ . Thus, if we replace  $\varepsilon(\Omega, \bar{\lambda})$  by  $\varepsilon(\theta, \bar{\lambda})$  in Eq. (18) and if we consider moreover that  $\frac{z}{2\rho} \varepsilon \tan \theta$  is small before unity, we can expand the exponential in the integral and get after some calculations

$$dn_{\gamma_e} \cong \frac{1}{2} n_{\gamma_0} \eta(\bar{\lambda}) [1 - \rho_F] e^{-\frac{z}{\Lambda_{core}(\bar{\lambda}) \cos \theta}} e^{-\frac{4}{\pi} \frac{z}{2\rho} \varepsilon(\theta) \tan \theta} \sin \theta d\theta \quad (19)$$

where the factor  $4/\pi$  is related to the extra-number of reflections of skew rays. Eq. (19) gives the attenuation for a particular class of rays and can be integrated over  $\theta \leq \theta_c$  in order to derive the number of photoelectrons detected at the fiber end.

In a previous paper [28] we have found that  $\varepsilon$  is proportional to the propagation angle  $\theta$

$$\varepsilon(\theta) \approx a\theta \cong a \tan \theta. \quad (20)$$

This relation will be checked experimentally in section 4. Substituting Eq. (20) into Eq. (19) and assuming that  $z/\Lambda_{core} \ll 1$  and  $za \tan^2 \theta_c \ll 2\rho$ , both exponentials can be expanded and we get finally the approximation

$$n_{\gamma_e} \cong \frac{n_{\gamma_0}}{2} (1 - \cos \theta_c) \eta(\bar{\lambda}) [1 - \rho_F] e^{-\frac{z}{\Lambda_{eff}}} \quad (21)$$

where

$$\frac{1}{\Lambda_{att}} = \frac{1}{\Lambda_{core}(\lambda)} \frac{1}{\cos \bar{\theta}} + \frac{4}{\pi} \frac{\varepsilon(\bar{\theta}) \tan \bar{\theta}}{2\rho} \quad (22)$$

and

$$\bar{\theta} = \frac{\theta_c}{\sqrt{2}} \quad (23)$$

We recognize in the factor  $\frac{1}{2}(1 - \cos \theta_c)$  the trapping efficiency of the fiber relative to bound rays and, in the global attenuation length  $\Lambda_{att}$ , a first term related to core losses and a second term due to interface losses.  $\bar{\theta}$  can be interpreted as a mean propagation angle and is equal to  $15.12^\circ$  in a PS/PMMA fiber. The factor  $\sqrt{2}$  in Eq. (23) depends weakly on the model which describes the angular variation of  $\varepsilon$ .

Taking  $\Lambda_{att} \cong +\infty$  in Eq. (21) and assuming that  $E_\gamma$  is in the 100eV-150eV range, we expect  $n_{pe} \cong 10 - 13$  ph.el./mm for a perfect PS/PMMA fiber readout by a standard bialkali photocathode with  $\eta(450 \text{ nm}) \cong 20\%$ .

It is interesting to compare the approximation given by Eq. (21) with the direct numerical integration of Eq. (18). For realistic values as for instance  $\Lambda_{core} = 3 \text{ m}$ ,  $a = 15 \cdot 10^{-4}$  and  $\rho = 0.45 \text{ mm}$ , it can be shown that the agreement between both expressions is excellent and leads to errors less than 2%. Eq. (21) predicts a logarithmic decrease of fiber signal as a function of fiber length but it must be stressed that the tunnelling rays which have certainly a different attenuation behaviour have been neglected, that a z-stationary light emission has been assumed and that we have moreover excluded cladding rays which contribute to light yield in the first tens of cm. As a result, Eq. (21) will not be representative of short fiber behaviour but it will be seen that it modelizes correctly the attenuation in the 0.5 m-3 m range.

### 3. Test of a PS/PMMA technology

In order to evaluate the performance of our PS/PMMA technology, we have decided to draw more than 60 km of scintillating fibers and to measure the optical properties at the different steps of the production.

In a preform technology, the fiber fabrication starts with the polymerization of individual PS rods. We had a polymerization run each week which yields 6 different PS rods. After the drawing, a rod, 400 mm in length and 40 mm in diameter, yields around 600 m of 1 mm fiber. In order to get a total fiber length of 60km, it required at least 10 polymerization runs. They have been spread over 6 months.

The fibers have a 0.9 mm scintillating PS core surrounded by a 500  $\mu\text{m}$  PMMA cladding. The efficient fraction of the fiber is not more than 81% due to the fact that our preform/tube technology had been initially developed for plastic microfibers which required a thick initial cladding tube [9]. Of course, the use of thinner PMMA tubes will increase the efficient part of fibers.

As far as possible we have kept constant the experimental conditions during the test. However, some problems encountered with our styrene supply required a slight change of the monomer purification. Some differences observed in the rheological behaviour of the polymer also required an adaptation of the drawing temperature. Every change has been recorded in order to allow a further analysis.

### 3.1 Choice of scintillator composition

We had to choose between binary scintillators as for instance PS+PBBO or PS+TPB, already studied for the fabrication of microfibers, and ternary scintillators as for example PS+bPBD+dPOPOP previously used for the manufacturing of the UA2 fibers. We already had fabrication reference with this last scintillator used with the previous PS/PVA technology and we decided to keep it in order to enable a comparison.

In the UA2 fibers the bPBD concentration was 1% in mass and the dPOPOP one 0.02%. The analysis presented in section 2.2 has already shown that the radiative transfer length is around  $\Lambda_{xy} = 300 - 400 \mu\text{m}$  with this dPOPOP concentration. That is hardly sufficient in 1 mm fibers. In UA2 fibers the aluminium sputtering prevented Y photons from escaping, but for the test we preferred to increase by a factor of 2.5 the dPOPOP concentration. The measurement of the mean transfer length yields  $\Lambda_{xy} = 140 \mu\text{m}$  for this concentration. A simple Montecarlo calculation which takes into account the light trapping at the core/cladding and at the cladding/air interfaces shows that the fraction of escaping Y photons is negligible in this case. Moreover, as discussed in section 2.2, we do not expect that the increased concentration will cause a significant additional core absorption.

### 3.2 Fabrication process

The fabrication of plastic scintillating fibers is difficult since it involves a large number of steps which require a clean environment, a long time and a constant care. We detail hereafter the technology developed and used at Saclay. It must be stressed that this technology is a laboratory one and can probably not compete with an optimized industrial technology. Nevertheless, our process can give a good idea of the problems encountered with the fabrication of plastic scintillating fibers.

#### 3.2.1 Purification

The first step is to prepare a very pure solution of fluorescent dyes in styrene monomer. The purification is a critical operation that will avoid many further troubles, as degassing for instance.

Commercial styrene contains many organic impurities as ethylbenzene, cumene, alphasethylstyrene and water. It also contains anti-polymerization agents (4-tert-butylcatechol) which inhibit the polystyrene formation. To purify the monomer we use the following process:

i) *Purification of styrene* on  $\text{Al}_2\text{O}_3$  pearls previously degassed at 100 °C.  $\text{Al}_2\text{O}_3$  removes water and polymerization inhibitors. This operation takes around 16 days at 5 °C under vacuum.

ii) *Filtering of styrene* on a 0.2  $\mu\text{m}$  filter in order to remove dust particles due to  $\text{Al}_2\text{O}_3$ .

iii) *Styrene distillation* under a 40 mm Hg vacuum in an inert  $\text{CO}_2$  atmosphere. Oxygen is a contaminant during all the purification process since styrene oxydation leads to a yellow coloring of polystyrene resulting in a low transparency over the blue region of the visible spectrum. The distillation

rate is about 2 l/hour and the temperature is kept constant at 60 °C in order to avoid the initiation of polymerization.

iv) *Purification of the dopants.* The commercial powder is placed in a clean erlenmeyer and the temperature is raised above the sublimation point. The purified powder is collected on the walls of the container, weighted and dissolved in a small amount of purified styrene in order to get a concentrated solution.

v) *Preparation of the polymerization ampoules.* The ampoules used for the polymerization have an external diameter of 38 mm and consist of a cylindrical part, 73 cm in length, followed by a 26 cm nozzle. The ampoule thickness is around 1.6 mm. The ampoules are very carefully washed with fluorhydric acid and rinsed out with water. After drying by adding ethanol and methylethylketone, the ampoules are degassed under vacuum, filled with Argon and carefully sealed. Before their use they are treated with a 1% dimethylchlorosilane solution in chloroform in order to get a Langmuir layer that prevents polystyrene adherence.

vi) *Preparation of fluorescent styrene.* The ampoules are pumped under vacuum at the end of the distillation column and filled with the concentrated fluorescent solution (iv). They receive directly the distilled styrene. After pumping at low temperature to degas again the purified monomer without starting the polymerization, the ampoules are slowly raised to ambient temperature and shaken in order to get an homogeneous mixture. Finally they are sealed under vacuum and stored for a few hours in a cold and dark place.

### 3.2.2 Polymerization

The polymerization process leads to long repetitive carbon structures due to the reaction of the unsaturated links of polymer molecules. This formation depends strongly on the temperature and on UV radiations. In polystyrene, the polymerization is an exothermic reaction and diverges rapidly after an initiation caused by temperature or by free radicals. To get a high quality polymer we have chosen to avoid polymerization initiators and to perform the reaction under vacuum with an external temperature control.

The polymerization process begins less than 24h after the filling of the polymerization ampoules. The reaction takes place in a furnace where the temperature is controlled at the 0.5°C level and follows the 5-days cycle described hereafter:

- i) During the first part the temperature is raised rapidly to 90°C and kept constant for 20 h.
- ii) The temperature is then gradually raised to 170 °C (21 h) and kept there for 10 h to complete the polymerization.
- iii) The temperature is then slowly decreased and the nozzles at the top of the ampoules are broken at 160 °C to increase the pressure in the ampoules.
- iv) Finally the temperature is decreased until it reaches the ambient temperature (54 h).

In order to get a good polymerization and a nice look of PS rods, two different problems have to be solved during the process:

- i) *Exothermy.* The polymerization reaction can be accelerated by two heat sources. The first one is related to the furnace temperature and is well controlled but the other one, related to the exothermy of

the reaction, is more difficult to predict. If the speed of the reaction becomes very high due to a rapid rise of the oven temperature at the beginning of the process, we have observed hot points in many parts of the ampoule that extend rapidly and lead to exothermic bubbles. In this case, many free radicals are formed and the monomer is rapidly transformed resulting in short polystyrene chains which present a very dispersive molar mass increasing the Rayleigh diffusion in the polymer. On the other hand, very long polystyrene chains would require a high drawing temperature that could lead to cladding damage. The polymerization exothermy must be rigorously controlled especially at the beginning of the reaction in the range between 90°C and 110°C. We have found an optimum with a polymer molar mass around 125000 resulting in a low dispersive material that can be drawn around 200°C. We have adapted consequently the preceding temperature program. During the polymerization, many sensors record the external temperature of each ampoule. A safety control is also incorporated in order to interrupt the polymerization if a high exothermy is observed. This protection was recognized necessary after a polymerization divergence.

ii) *Polymer compression.* The volume of a given mass of polystyrene is 17% lower than the equivalent mass of the monomer. If the material contraction is not controlled, we have observed bubbles in the PS rods which appear during the temperature decrease. The Langmuir coating deposited on the ampoules prevents PS adherence and avoids partly the problem. Nevertheless the compression must be controlled. For this purpose, the polymerization ampoules are reversed (nozzle down) at the beginning of the reaction. The nozzles are broken during the temperature decrease at 160°C after a reversal of the ampoules. The pressure difference between the two ends of the rods and the viscosity of polystyrene at this temperature ensure the compression of the polymer and avoid bubble formation in the middle of the rods.

### 3.2.3 Fiber drawing

#### *i/ Preparation of PS rods*

After the removal of PS rods from the polymerization ampoules, their look is far from that required for a good preform. We often observe bubbles at one end of the rods and many scores on the surface. To increase the quality of the interface between PS and cladding and to prepare the drawing, we have to machine and to polish the rods.

All the following operations including the storage require many precautions since dust and organic impurities would disturb the drawing process, causing either irregularities in fiber diameter or degassing of the preform.

The PS rods are first machined to form a cylindrical part, 35 mm in diameter, with a small conical part at one end of the rod. The fixing of the rod to the drawing system is also prepared at this stage. The rods are then rubbed with various abrasive papers and carefully cleaned with water.

After drying at 65 °C during 3 days, the rods are chemically polished. This operation ensures a very smooth surface and removes moreover the polystyrene molecules damaged by the mechanical machining. The solvent is simply a solution of styrene that still contains inhibitors. The rods are partly plunged in the monomer and are turning horizontally around their axis during a few minutes. After this operation, the surface looks very nice but the solvent which has diffused in the polymer must be removed. Thus, the rods are placed in a ventilated oven at 70 °C during 3 days in order to remove the

monomer or to fix it on the polystyrene chain. A correct drying prevents the degassing during the fiber drawing.

### ii/ Preparation of the cladding tubes

Our technology requires that PMMA tubes surround the 35 mm diameter PS rods during the drawing process. The commercial extruded tubes have a  $36 \pm 0.25$  mm inner diameter and a 2 mm thickness. The matching between preform and tube diameter is of great importance since an excessive gap causes a cladding pleating during the drawing.

The tubes are cut to the preform size and the protection paper is removed. They are carefully washed with distilled water both internally and externally in order to avoid dust trapping at the core/cladding interface. They are then placed in an oven during 3 days at 65 °C and pumped in order to remove water which is easily absorbed by PMMA and could perturb the fiber drawing by absorption of IR radiation.

### iii/ Fiber drawing

The drawing station is shown schematically in fig. 7. The PS rod and the PMMA tube are centered at the top of the drawing oven and the interface is pumped under primary vacuum during the whole process. Both are fixed on a common system that ensures a very regular and vibrationless descent in the furnace with a 7 mm/minute speed.

The first part of the oven ensures a first rise of the temperature with help of a toroidal electrical resistance. The heating is performed in the second part by 6 equally spaced 150 W IR lamps. The cylindrical oven has a 200 mm diameter and the copper walls are carefully polished and regularly cleaned. Copper is a good reflector for IR but is progressively damaged by the degassing of the preforms. The lamps emit in the 0.8 and 1.6  $\mu\text{m}$  range and provide an uniform heating of the preform core. The temperature is measured with a pyrometer and controlled by the variation of lamp power.

When the temperature of the preform increases, both PS and PMMA materials soften and tape into a fiber. A nitrogen laminar flux is circulating in the 4 m long descent column and in the oven in order to ensure a progressive cooling of the fiber and prevent PS oxydation. The end of the fiber is affixed to a winding drum which is driven by a motor. A capstan ensures the regulation of the descent speed.

The fiber diameter is measured optically with a precision of 0.5  $\mu\text{m}$  at the bottom of the column and the strain of fiber material is observed by polarimetry.

In order to get a regular fiber drawing, the descent speed of the preform, the descent speed of the fiber, the temperature in the oven, the fiber diameter and the fiber strain have to be controlled simultaneously. In stationary operating conditions, the fiber diameter depends only on the descent speeds and is given by

$$\Phi_{fiber}^2 = \Phi_{preform}^2 \frac{v_{preform}}{v_{fiber}} \quad (24)$$

The temperature is adjusted in order to reduce the fiber strain. With good PS rods, furnace temperatures of 205°C have been observed. The fiber diameter is constant at the ±1% level.

Finally it must be stressed that fiber drawing requires a long expertise since many parameters with long time constant have to be controlled simultaneously and adjusted to the rheological behaviour of preforms.

### 3.3 Systematic measurements

#### 3.3.1 Preform measurements

Systematic optical measurements have been performed at the different steps of the fabrication. Before the machining and the surfacing operations, we measure the optical transparency of the 6 PS rods produced during the same polymerization run. A rod is designated hereafter by three numbers N\_W\_Y (Y is a code for the year, W is the week of production and N a number which distinguishes the rod in the bunch).

After a careful polishing of both ends, the PS rods, 40 mm in diameter, 400 mm in length, are measured with the experimental setup shown in fig. 8. The halogen light source of a Guided Wave Inc. spectrometer is coupled to a quartz fiber, 500 μm in diameter, set at the focal point of an achromatic lens in order to get a 10 mm parallel beam. The spectrum of the light ranges from 400 nm to 900 nm. A second lens collects and injects the transmitted beam in a fiber coupled to a remote controlled monochromator. The preform rod is placed between the two lenses and both faces are optically coupled to quartz windows in order to avoid any trouble with the polishing of the rod edges and to reduce the effect of PS refractive index dispersion.

A typical transparency spectrum (air is taken as reference) is plotted in Fig. 9. We recognize the IR absorption bands of PS and we observe an important increase of the absorption in the blue-UV range which is mainly due to polystyrene and can be observed in clear preforms as well. However, the fluorescent dopants also contribute to the absorption in this spectral range which is of particular interest in respect to fiber properties since it corresponds to dPOPOP emission.

To increase the precision of the measurement, we have compared the spectrum obtained with the rod to a reference spectrum measured with a short 10 mm sample cut in the same rod. This procedure allows a complete correction of the dispersion of PS. The absorption coefficient is given by

$$\alpha_{rod}(\lambda) = \frac{-1}{L_{sample} - L_{ref}} \ln \left[ \frac{I_{sample}(\lambda)}{I_{reference}(\lambda)} \right] \quad (25)$$

where  $I_{sample}$  and  $I_{reference}$  are the light intensity transmitted by the rod and the reference. Following this procedure, the precision on the estimation of  $\alpha_{rod}$  is better than 0.1 m<sup>-1</sup> over the spectral range from 440 nm to 800 nm. Due to absorption, the precision decreases in the blue part of the spectrum.

We have polymerized a total of 60 rods. 34 were bubbleless and have been measured using the above procedure. The remaining rods did not allowed significant measurement and most of them have not been



drawn later. The absorption coefficient is measured at different wavelengths. Fig. 10 presents all the 34 measurements plotted together in order to give a qualitative idea of the process reproductibility.

Most PS rods exhibit more or less the same behaviour but 8 are outside the standard deviation. Important differences also appear in the range between 420 and 450nm. Part of this effect is related to the uncertainty in measurements but we have also observed a correlation to problems encountered during the polymerization. In this case which corresponds to 3 bunches out of 10, the rods exhibit a strong yellow coloring. For one bunch (week 50), 2 rods have a normal behaviour whereas the 2 remaining are very diffusing. We have not found satisfactory explanation of this difference. Finally, it should be noted that only 4 polymerization runs were satisfactory in terms of production yield and of optical quality.

### 3.3.2 Fiber measurements

After the fiber drawing, 10 samples are randomly cut on the storage drum. The light yield and the attenuation are measured with the apparatus described in fig. 11.

The optical fiber is placed in a V-guide and excited laterally by a 1 mm collimated  $^{90}\text{Sr}$  source which emits electrons of mean energy equal to 2.28 MeV. The source travels above the fiber in order to vary the distance  $z$  between excitation point and fiber end in the range between 0 m and 2 m. The 10 mm gap between the fiber and the source is kept constant at the 1% level during the displacement. We measure the current delivered by a Philips XP2262B photomultiplier coupled to a 100 mm long PMMA guide wrapped with an aluminium foil. The PMT power supply is stable at the level of 0.1%.

The fiber end readout by the photodetector is very carefully polished whereas the opposite face is kept rough in order to avoid parasitic reflections. For standard measurements, the fibers are not optically coupled to the PMMA guide.

We have measured independantly the angular response of the detecting system (PMT+guide). It is plotted in Fig. 12. The variation is less than  $\pm 8\%$  in the N.A. of the fiber ( $-36^\circ$  to  $+36^\circ$ ). The quantum efficiency, plotted in fig. 13 is estimated from a direct measurement of guide transparency and from the quantum efficiency of the PMT given by the manufacturer. Over the emission of blue fibers, the integrated efficiency is around 20%.

The source has a 30 y half life and the setup is calibrated before each measurement with one scintillating aluminized fiber previously calibrated in a particle beam. In table 4, we have compared the results of beam calibration to the measurements performed with the above setup. They are in good agreement and allow the conversion of PMT current in photoelectrons units. An other correction must also be applied in order to take into account the core diameter of the fibers. The tested fibers have a 0.9mm core whereas the calibration fibers have a 1mm core. Since the fiber cross section is uniformly irradiated by the source, the correction scales as  $\phi^2$ .

This procedure is quite simple. We have estimated that the precision of relative measurement is at the level of 2% for source position after 0.5 m. This estimation takes into account the fiber polishing always performed by the same operator and all other error as the fiber positioning for instance. However, it must be stressed that the calculation of the absolute efficiency is certainly less accurate than with other

setups which use photon counting [29] but which are more difficult to implement for routine measurements.

A typical measurement is shown in Fig.14 for the 10 fibers derived from the preform 4\_49\_0. For source positions after 0.6 m, the dispersion is small but increases at short distance due to the cladding rays which are very sensitive to the quality of the cladding-air interface. Between 0.6 m and 2 m a single exponential

$$y(z) = y_0 \cdot e^{-z/\Lambda_{att}} \quad (26)$$

can be fitted to the measured values.  $\Lambda_{att}$  is the attenuation length and  $y_0$  the extrapolated light yield at  $z=0$  m. From fig. 14, we get  $\Lambda_{att}=2.36\pm 0.2$ m and  $y_0=11.0\pm 0.73$ ph.el./mm. The value of  $y_0$  is in agreement with the predicted value given in section 2.4 (10-13 ph.el./mm).

In order to check the stability of both apparatus and fiber properties, we have performed systematic measurements during the month following the drawing. The light yield measured at  $z=1$ m is plotted in Fig. 15 for the 1\_49\_0 and 3\_49\_0 fibers. These measurements are very close together. That shows not only the good stability of fiber properties over the whole preform but also the absence of fiber ageing in the few weeks after fabrication.

We have plotted in Fig. 16 the light yield and the attenuation length of the fibers derived from the various preforms. Each point represents the mean properties of the 10 random samples. These measurements have been compared to the corresponding measurements of the rods. For 3 preforms designated by 6\_48\_0, 6\_50\_0, 3\_50\_0 the poor quality of the fibers can be related to an important preform absorption. For the remaining samples, we have not found a strong correlation between the rod measurement and the fiber properties. For example, the fibers polymerized during the week 49 exhibit excellent properties (attenuation length greater than 2 m and more than 6 ph.el./mm@1m) but the corresponding rods were not very different from those produced during the week 03 which have led to mediocre fibers. Furthermore, we are unable to explain the dispersion between the measurements of the fibers derived from the rods of week 51 which were optically close and have followed exactly the same manufacturing process.

### 3.3.3 Discussion

From the measurements plotted in fig. 16, we can estimate the mean properties of the fibers. We find a mean attenuation length of  $1.9\pm 0.2$  m and a mean light yield of  $5.36\pm 0.6$  ph.el./mm@1m. In term of attenuation, the PS/PMMA fibers are very close to those produced with the previous PS/PVA technology for the construction of the UA2 detector. The mean light yield is 20% higher. This can be explained by the scintillator formulation which ensures a better energy transfer in the fiber core.

We have also compared the fibers produced at Saclay with other commercial blue fibers using the same setup and the same polishing procedure. The measurements reported in fig. 17 concern fibers provided in 1991 and do not prejudice the improvements which have probably been achieved by the different manufacturers since this date. A typical Saclay fiber such as 3\_42\_01 is comparable to the commercial fibers and is at the level of the UA2 aluminized fiber. The 3\_49\_05 fiber is significantly better (around 30%) but unfortunately as mentioned previously we cannot explain this excellent

behaviour in term of manufacturing process. Nevertheless, fig. 17 shows that the PS/PMMA technology is competitive as far as optical property is concerned. It also indicates that the commercial standard can probably be increased in order to reach the properties observed in the 3\_49\_0 fiber.

#### **4. Light losses in scintillating fibers**

Until now, we have focussed on the global properties of the fibers which do not allow to separate between the different loss factors. We report hereafter more specific measurements performed on PS/PMMA fibers which better explain the fiber behaviour.

##### **4.1 Cladding light**

In order to precise the influence of cladding light, we have used the procedure proposed by Hawkes [29]. The end of the fiber is cast into a PS disc and glued with a material which has a refractive index higher than PS. The disc, 40 mm in diameter and 5 mm in length ensures the refraction of the light which is propagating in the cladding. Cladding rays are thus spatially separated from core rays.

The measurements have been performed with the experimental setup of Fig. 11 modified in order to enable the introduction of a small diaphragm, 5 mm in diameter, at the entrance of the PMMA guide. This diaphragm rejects the cladding rays refracted in the disc and the intensity difference between the non-diaphragm and diaphragm measurements gives directly the cladding light contribution. That is plotted in fig. 18. We observe that cladding rays have a very short attenuation length and do not contribute significantly to the fiber emission after 0.6 m as postulated previously. However a small residual part results in a systematic 5-10% error in the calculation of the attenuation length.

We also note in Fig. 18 that the core light selected by the diaphragm exhibits nevertheless a non exponential behaviour at short distance which cannot be explained this time by cladding rays. It may be interpreted either as an effect of spectral variation of fiber emission and/or as the result of tunneling rays attenuation.

##### **4.2 Core losses measurements**

In order to study the core losses in scintillating fibers we have used the experimental setup described in Fig. 19. The scintillating fiber is excited laterally at a distance  $z$  from the fiber end by a quartz fiber coupled to a monitored UV light source. The fiber emission is analyzed by a Jobin Yvon monochromator in order to select a particular wavelength. The slits of the monochromator select a small angular solid angle in fiber emission. The emission of the fiber, integrated over the full spectral range is compared in Fig. 20 with the corresponding attenuation measurement performed with the attenuation bench of fig.11 modified in order to select a small angular cone of fiber emission ( $0^\circ$ - $10^\circ$ ). The agreement between both measurements is quite satisfactory and permits to be confident in the UV results.

In Fig. 21 we have plotted the emission spectra of the 1\_49\_01 and 6\_48\_02 fibers measured at various excitation distance. For both fibers, the spectral shift is important in the first tens of cm. At short distance we recognize the dPOPOP emission peaking at 430 nm but after 0.5 m the maximum shifts to 460 nm and does not vary very much after this distance. As a result we can consider that fiber emission is homothetical in the 0.5m-2m range. This observation gives an experimental justification for the

assumption made in section 2.4. Furthermore, since the left part of the spectrum is filtered over short distances, we explain the non exponential behaviour of fiber light yield and we also understand the 25% discrepancy between the value predicted by Eq. (21) and the value  $y_0$  deduced from the fit of a single exponential between 0.6 m and 2 m.

At a given wavelength, the decrease of spectral intensity is directly related to the absorption coefficient  $1/\Lambda_{core}(\lambda)$  of the fiber core. It can be compared to the absorption of the PS rods measured before the fiber drawing. We observe in Fig. 22 that for both 1\_49\_0 and 6\_48\_0 fibers, the measurements are compatible. This result is easily explained for the 6\_48\_0 rod which exhibited a strong initial attenuation that cannot be very much increased during the drawing. However, we expected to see a more significant effect in the 1\_49\_0 fiber which is derived from a very transparent rod but this is not observed in fig. 22 except perhaps at 450 nm.

With regard to fiber fabrication, this is an important result which indicates that the attenuation of the fiber core is not increased by the drawing operation and thus can be further improved by a better control of the purification and of the polymerization process.

### 4.3 Interface losses measurements

In order to fully validate the previous conclusion, we have checked that the interface losses are small as compared to the core losses. Many studies of reflection losses have already been reported [28, 30-32] but were performed with lasers and not under real operating conditions. We propose hereafter to modify slightly the setup described in Fig. 11 in order to achieve this measurement. The basic idea is to select an emission cone at the end of the fiber and to get the attenuation of the different angular components.

This is achieved by a diaphragm,  $\phi=13$  mm in diameter, placed at the entrance of the PMMA guide. The detecting system is moved away from the fiber end with a gap  $e_i$  which can vary from 0 to 20 mm. We have performed the measurement for 6 positions ( $i=0..5$ ) equal to 0, 5, 7.5, 10, 15 and 20 mm. For a given gap  $e_i$ , the PMT detects the amount of photoelectrons  $n_i(z)$  emitted in the cone limited by the propagation angle

$$\theta_i = a \sin \left( \frac{1}{n_{co}} \frac{(\Phi / 2e_i)}{\sqrt{1 + (\Phi / 2e_i)^2}} \right) \quad (26)$$

From the difference between two successive measurements, we can define the corrected value

$$\delta n_i = \frac{2}{\eta_i + \eta_{i-1}} [n_i(z) - n_{i-1}(z)] \quad (27)$$

where  $\eta_i$  is the relative detector efficiency measured at the incidence which corresponds to the refraction of  $\theta_i$  at fiber end (see fig. 12).

According to Eq. (19) we have within the numerical aperture and after  $z=0.6\text{m}$

$$\delta n_i \cong \eta(\bar{\lambda}) \frac{1}{2} n_{\gamma 0} [1 - \rho_F] \int_{\theta_{i-1}}^{\theta_i} e^{-\frac{z}{\Lambda_{core}(\bar{\lambda}) \cos \theta}} e^{-\frac{4z}{\pi 2\rho} \varepsilon(\theta) \tan \theta} \sin \theta d\theta \quad (28)$$

Providing that the angular range between  $\theta_i$  and  $\theta_{i-1}$  is small, the above integral can be approximated by

$$\delta n_i \cong \delta n_{io} e^{-z/\Lambda_{att}(\bar{\theta}_i)}. \quad (29)$$

$\bar{\theta}_i$  is the mean propagation angle defined by

$$\bar{\theta}_i = \frac{\theta_i + \theta_{i-1}}{2}, \quad (30)$$

$\Lambda_{att}(\bar{\theta}_i)$  is the attenuation length given by

$$\frac{1}{\Lambda_{att}(\bar{\theta}_i)} = \frac{1}{\Lambda_{core}(\bar{\lambda}) \cos \bar{\theta}_i} + \frac{2}{\pi \rho} \varepsilon(\bar{\theta}_i) \tan \bar{\theta}_i \quad (31)$$

and  $\delta n_{io}$  is the light yield at origin that can be expressed as

$$\delta n_{io} = \frac{1}{2} n_{\gamma 0} \eta(\bar{\lambda}, \bar{\theta}_i) [1 - \rho_F] [\cos \theta_i - \cos \theta_{i-1}] \quad (32)$$

We have fitted Eq. (29) to the corrected differences  $\delta n_i$  measured on various PS/PMMA and PS/PVA fibers. We define for each propagation angle a value  $\delta n_{io}$  and  $1/\Lambda_{att}(\bar{\theta}_i)$  which is plotted in fig. 23 for the 4\_49\_0 fibers and in fig. 24 for the PS/PVA fibers. As expected, we note an increase of the absorption as a function of the propagation angle. The curves of figs 23 and 24 have been fitted by Eq. (31) assuming that  $\varepsilon$  is proportional to  $\bar{\theta}_i$  as described by Eq. (20). That yields the estimation of  $a$  and of  $\Lambda_{core}(\bar{\lambda})$  given in table 5.

We have also calculated the attenuation length equivalent to the interface losses that can be expressed as

$$\frac{1}{\Lambda_{interface}} = \frac{4}{\pi} \frac{a \tan^2 \bar{\theta}}{2\rho} \quad (33)$$

where  $\bar{\theta}$  is defined by Eq. (23). In all the fibers that have been studied, the attenuation from core losses is predominant but presents a large dispersion since it ranges from 2 m in the 3\_51\_0 fiber to 3.4 m in

the 4\_49\_0 fibers. The fitted absorption coefficients  $\alpha_{core} = 1 / \Lambda_{core}$  are in good agreement with the rod absorption measured at 460 nm with the setup of fig. 8. This means that the above dispersion is really related to the polymer transparency and not to the drawing process. On the other hand, It must be noted that most PS/PMMA fibers present a better transparency than PS/PVA fibers. This shows that the care taken during this test in order to get a high purified monomer is certainly useful.

The interface losses described by the parameter  $a$  are significantly higher in the *PS/PMMA* fibers than in the *PS/PVA* fibers. This time again, we note a large dispersion between the fibers. The 4\_49\_0 fibers is not far from the UA2 fibers with  $a \cong 1.23 \pm 0.19 \cdot 10^{-3} \text{ rad}^{-1}$ . On the contrary, the 4\_42\_0 and 1\_42\_0 exhibit interface losses 50% higher. We have no complete explanation of this difference but we have noted that the drawing temperature and the fiber strain were higher for these two preforms (215°C instead of 207°C). It must be stressed that the order of magnitude of the deviation to total reflection is in good agreement with previous measurements performed with a laser source [28].

In the two last columns of table 5, we have compared the attenuation length deduced from the core and interface losses to the value obtained with direct measurements at full fiber aperture (see section 3.2). The agreement is quite satisfactory and shows that the fiber behaviour is correctly described by the model of section 2.4.

Finally, as reported in a previous paper [27], we can also use the corrected differences  $\delta n_i(z)$  to get the amount of photoelectrons emitted inside the solid angle  $\Omega_i = 1 - \cos(\theta_i)$

$$n(\Omega_i, z) = \sum_{k=0}^i \delta n_k(z). \quad (34)$$

This is plotted in fig. 25 for the 4\_49\_0 fibers at various excitation distance  $z$ . We can estimate that tunneling rays represent less than 25% of light yield after  $z=1\text{m}$ . However, since the values reported in fig. 25 have been corrected from the PMT angular response, the effective contribution of tunneling rays to the light detected by the PMT is not more than 15%. That validates the assumption made in section 2.4 on tunnelling rays. On the other hand, we note that for small  $\Omega_i$ , the light yield is proportional to  $\Omega_i$ , as expected from the isotropy of scintillation. According to Eq. (19), the slope of the curve around  $\theta \cong 0$  can be expressed as

$$\frac{dn(\Omega, z)}{d\Omega} = \frac{1}{4\pi} n_{\gamma_0} \eta(\bar{\lambda}) (1 - \rho_F) e^{-z/\Lambda_{core}(\bar{\lambda})} \quad (35)$$

and is independant of reflection losses. Thus, the evolution of the slope as a function of the distance  $z$  yields an independant estimation of core attenuation  $\Lambda_{core}(\bar{\lambda})$ . This value which also corresponds to the propagation angle  $\theta = 0$  has been plotted in figures 23 and 24 and is in good agreement with the other measurements.

## 5. Conclusion

We have presented the technology developped at Saclay for the fabrication of plastic scintillating fibers. The fibers result from the assembly of a PMMA tube and of a doped PS rod obtained after the purification of commercial styrene followed by a thermal polymerization. The scintillator composition

has been discussed. For the technological test reported in this paper we have chosen a standard ternary scintillator composed of bPBD (1%) and dPOPOP (0.05%). By means of optical measurements performed at various steps of the fabrication, we have carefully studied 10 fabrication bunches. Out of the 60 rods which have been produced, 23 have given satisfactory fibers. The mean attenuation length is  $1.9 \pm 0.2$  m, at the level of the fibers manufactured for the UA2 detector with a PS/PVA technology. An optimisation of the dPOPOP concentration has ensured a 20% increase of light yield resulting in  $5.36 \pm 0.6$  ph.e.l./mm@z=1 m. These properties are at least equivalent to those measured with commercially available fibers.

An experimental study has been achieved in order to explain the attenuation behaviour of the fibers. During the first 0.6 m, the light propagation is perturbed by the cladding rays and by the spectral shift of fiber emission. After 0.6 m, the behaviour is more stationary with an emission peaking at 460 nm and the fiber is correctly described by a simple model including core and interface losses and limited to the fiber numerical aperture.

We have compared the attenuation measured in the fiber core with the corresponding attenuation of the initial PS rods. Both measurements are very close, showing that the polymer transparency is not significantly damaged by the drawing process.

The interface losses have been measured with a setup which reproduces the operating conditions of the fibers and uses particle excitation. In good agreement with previous measurements performed with a laser source, we have checked that the deviation to total reflection is proportional to the propagation angle in the fiber. At  $15.11^\circ$ , which is the mean propagation angle in PS/PMMA fibers, the loss per total reflection is around  $10^{-4}$ , slightly greater than in PS/PVA fibers. We have observed an increase of this loss as a function of the drawing temperature and of fiber strain. It must be stressed that in 1 mm diameter fibers the interface attenuation represents less than 30% of the global losses.

These results validate our new technology. In the best fibers, the scintillation yield is higher than with the previous PS/PVA technology. The slight increase of the interface losses are compensated by a better core transparency and the cladding thickness can be adapted in order to enable the fabrication of small diameter fibers. On the other hand, the low global yield of the process (around 40%) appears as the weak point of the fabrication. It is due to an inadequate control of thermal polymerization and could certainly be improved by further work. Nevertheless, this study has shown that the loss factors in scintillating fibers are well understood and that we cannot expect very important increase of fiber light yield. As a result we have estimated that further work on fiber fabrication is not within the expertise of a HEP research laboratory and we decided to stop our R&D program in this field.

## References

- [1] S.R. Borenstein et al. IEEE Trans. Nucl. Sci. NS-29 (1982) 402.
- [2] L.R. Allemand et al. Nucl. Instr. and Meth. 225 (1984) 522.
- [3] H. Blumenfeld et al., Nucl. Instr. and Meth. 225 (1984) 518.
- [4] H. Blumenfeld et al. IEEE Trans. Nucl. Sci. NS-33 (1986) 54.
- [5] R.E. Ansorge et al., Nucl. Instr. and Meth. A265 (1988) 33.
- [6] J. Alitti et al., Nucl. Instr. and Meth. A273 (1988) 135.
- [7] J. Kirkby, Proc. 5th Topical Workshop on pp Collider Physics, St Vincent, Aosta Valley (1985) 672

- [8] P. Rebourgeard et al. IEEE Trans. Nucl. Sci. NS-36 (1986) 150.
- [9] H. Blumenfeld et al. Nucl. Instr. and Meth. A278 (1989), 619.
- [10] P. Rebourgeard, Thèse de doctorat, Note CEA-N2657 (1991), in French.
- [11] C. Angelini et al., Nucl. Instr. and Meth. A 281 (1989) 50.
- [12] C. Angelini et al., Nucl. Instr. and Meth. A 289 (1990) 356.
- [13] C. Angelini et al., Nucl. Instr. and Meth. A 295 (1990) 299.
- [14] H. Leutz, Nucl. Instr. and Meth. A 364 (1995) 422.
- [15] V.M. Feygelman et al., Nucl. Instr. and Meth. A 290 (1990) 131-135.
- [16] I.B. Berlman, Handbook of fluorescence spectra of aromatic molecules (1971) Academic Press.
- [17] L. Basile, Trans. Faraday Soc. 60 (1964) 1702.
- [18] A. Hallam et al., J. Phys. B, Atom. Molec. Phys. 11, 18 (1978) 3273.
- [19] J.B. Birks, The theory and practice of scintillating counting (1964) Pergamon Press.
- [20] T. Förster, Ann. Phys. 2 (1948) 55.
- [21] T. Förster, Discussions Faraday Society. 27 (1959) 7.
- [22] C.L. Renschler and L.A. Harrah, Nucl. Instr. and Meth. A235 (1985) 41.
- [23] A.D. Bross, Nucl. Instr. and Meth. A295 (1990) 315-322.
- [24] A. Bertin et al. Note CEA-N-2482 (1986).
- [25] A.W. Snyder and J.D. Love, Optical Wave Guide Theory (1983) Chapman & Hall.
- [26] American Institute of Physics Handbook (Mc Graw Hill, 1972).
- [27] Ph. Rebourgeard et al., Trapping efficiency of plastic scintillating fibers. DAPNIA/SED 96-02, submitted to Nucl. Instr. and Meth.
- [28] H. Blumenfeld et al. Nucl. Instr. and Meth. A309 (1991) 169-178.
- [29] C.M. Hawkes et al. Nucl. Instr. and Meth. A292 (1990) 329-336.
- [30] C. D'Ambrosio et al. Nucl. Instr. and Meth. A306 (1991) 549-556.
- [31] J.T. Remillard et al. Appl. Opt. Vol. 31, No. 34, 7232-7241 (1992).
- [32] J. Dugas et al., Appl. Opt., Vol. 26, No. 19 (1987) 4198.
- [33] CMS Technical proposal, CERN/LHCC 94-38 (1994).
- [34] ATLAS Technical proposal, CERN/LHCC 94-43 (1994).
- [35] P. Annis et al. Nucl. Instr. and Meth. A367 (1995) 367-371.
- [36] D. Adams et al. IEEE Conference record Vol.1 (1994) 282-286.



Table 1. Properties of polymers used in the fabrication of plastic scintillating fibers.

Material	Use	Peak emission [nm]	Refractive index @450nm	Tg[°C]
Polystyrene	PS Core	305 (330 <sup>1</sup> )	1.613	94
Polymethyl methacrylate	PMMA Cladding	weak	1.502	100-110
Polyvinyl Acetate	PVA Cladding	weak	1.46	39

<sup>1</sup> In solution with toluene

Table 2. Optical properties of fluorescent molecules used in the elaboration of scintillating fibers.

Dopant	Molar mass [g]	Peak absorption [nm]	Peak emission [nm]	Quantum efficiency	Decay time [ns]
b PBD	354.5	305	365	0.51	1.83
POPOP	392	370	430	0.85	1.5
PBBO	347.4	328	395	0.79	2.1
PMP450	294	305	435	0.74	3.6
3HF	238	340	530	0.40	8
PTerphényl	230	275	340	0.93	0.95

Table 3. Parameters used in the model.

$n_{co}$	=	Refractive index of fiber core
$n_{cl}$	=	Refractive index of cladding
$n_a$	=	Refractive index of air
$n_e$	=	Refractive index of coupling between fiber end and photodetector
$\rho$	=	Core radius
$\rho_e$	=	External fiber radius
NA	=	Numerical aperture $=\sqrt{n_{co}^2 - n_{cl}^2}$
$\theta_{NA}$	=	Half angle of emission cone in air $=\sin^{-1}(NA)$
$r$	=	Distance to fiber axis
$\alpha$	=	Polar angle
$z$	=	Distance to fiber end
$\theta$	=	Propagation angle relative to the fiber axis
$\psi$	=	Azimuthal angle $\psi$ relative to the radial axis
$r_{ic}$	=	Closest distance of skew ray to fiber axis
$\theta_c$	=	Critical angle relative to core-clad interface $\cos^{-1}[n_{cl} / n_{co}]$
$\theta_a$	=	Critical angle relative to clad-air interface $\cos^{-1}[n_a / n_{co}]$
$\theta_e$	=	Critical angle relative to core-coupling interface $\sin^{-1}[n_e / n_{co}]$

Table 4  
Calibration of the fiber setup.

Fiber	Beam Calibration	Bench Measurement [a.u.]
UA2 ref_4	4.27 ph.el.	52±1
UA2 ref_10	4.50 ph.el.	57±1
UA2 ref_13	4.65 ph.el.	59±1
	1 ph.el.	12.5±0.1

Table 5. Measurement of core and interface losses.

Fiber type	Fiber designation	$\alpha_{core}$ [m <sup>-1</sup> ]	a [10 <sup>-3</sup> ]	$\Lambda_{core}$ [m]	$\Lambda_{interface}$ [m]	$\Lambda_{att}$ deduced from (Eq. 22) [m]	$\Lambda_{att}$ measured [m]
PS/PMMA	4_49_0	0.29±0.03	1.23±0.19	3.42±0.39	7.86±1.20	2.38±0.22	2.23±0.08
PS/PMMA	4_42_0	0.34±0.03	1.71±0.17	2.92±0.25	5.68±0.57	1.93±0.13	1.85±0.10
PS/PMMA	3_51_0	0.49±0.04	1.46±0.35	2.04±0.17	6.65±1.58	1.56±0.13	1.54±0.08
PS/PMMA	1_42_0	0.47±0.03	1.79±0.19	2.14±0.15	5.42±0.57	1.54±0.09	1.46±0.10
PS/PVA	UA2	0.45±0.01	0.97±0.08	2.22±0.06	7.89±0.68	1.73±0.05	1.65±0.09

## Figure Captions

- Fig. 1. Emission spectrum of undoped polystyrene [10].
- Fig. 2. Absorption of polystyrene measured in an undoped PS rod [6].
- Fig. 3. Influence of Förster's transfers on the quantum efficiency in PS+PBBO.
- Fig. 4. Emission spectrum of PS+bPBD[1%]+dPOPOP[0.2%] films [10].
- Fig. 5. Absorption and emission spectrum of POPOP.
- Fig. 6. Ray Parameters.
- Fig. 7. Fiber pulling station.
- Fig. 8. Setup for the measurement of PS rods.
- Fig. 9. Transmittance of a typical 400mm doped PS rod.
- Fig. 10. Absorption coefficients measured in the various PS rods.
- Fig. 11. Setup for the measurement of fiber light yield.
- Fig. 12. Angular response of the PMT associated with the PMMA guide.
- Fig. 13. Quantum efficiency of the PMT associated with the PMMA guide.
- Fig. 14. Measurements of the fibers issued from the 4\_49\_0 preform.
- Fig. 15. Variation of the measurements after the drawing.
- Fig. 16. Properties of scintillating fibers. Each point represents the mean values of 10 fibers.
- Fig. 17. Measurement of scintillating fibers from different origins.
- Fig. 18. Core and cladding light in a PS/PMMA scintillating fiber.
- Fig. 19. Experimental setup for the measurement of fiber emission spectrum.
- Fig. 20. Comparison of light and  $^{90}\text{Sr}$  source excitation
- Fig. 21. Emission spectra as a function of fiber length for 1\_49\_01 and 6\_48\_02 fibers. The spectra are measured at 0.1, 0.2, 0.5, 1, 1.5, 2 m. The maximum of emission shifts from 440 nm to 460 nm. After 0.5 m, the emission is almost stationary.

Fig. 22. Absorption of bulk material measured in scintillating fibers and in preform rods.

Fig. 23. Absorption measured in the PS/PMMA fibers derived from the 4\_49\_0 rod.

Fig. 24. Absorption measured in PS/PVA fibers.

Fig. 25. Angular distribution of light in PS/PMMA fibers.

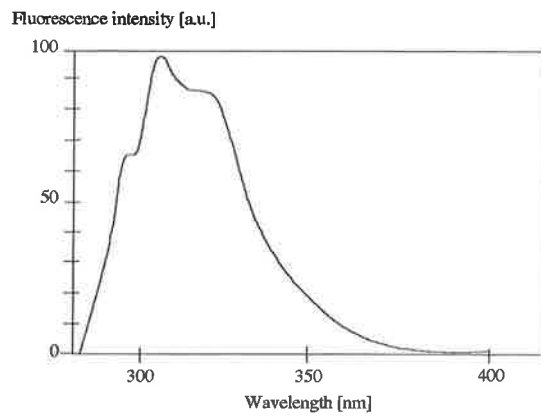


Fig. 1. Emission spectrum of undoped polystyrene [10].

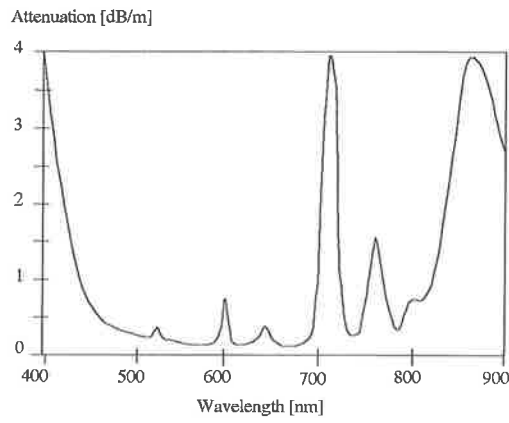


Fig. 2. Absorption of polystyrene measured in an undoped PS rod [6].

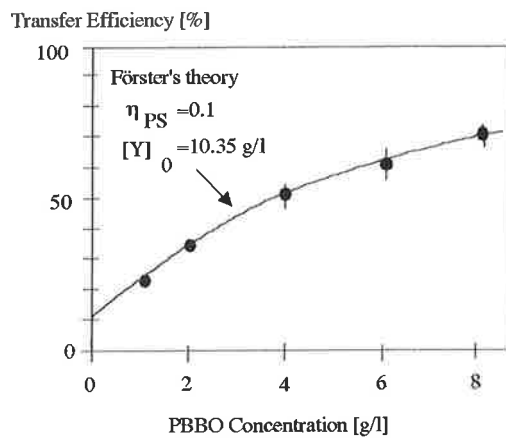


Fig. 3. Influence of Förster's transfers on the quantum efficiency in PS+PBBO.

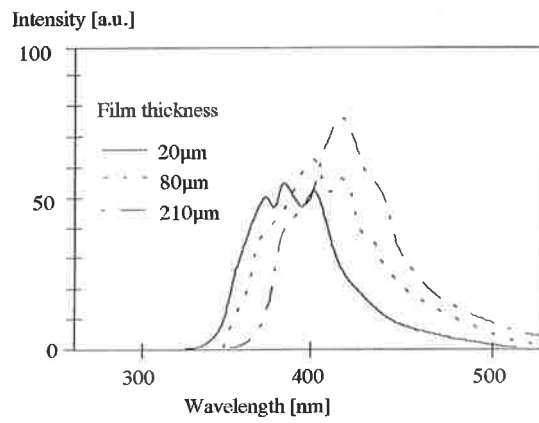


Fig. 4. Emission spectrum of PS+bPBD[1%]+dPOPOP[0.2%] films [10].

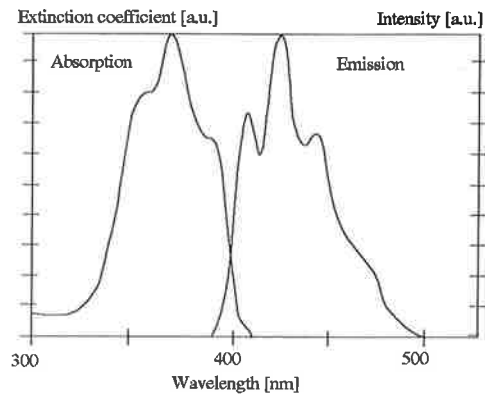


Fig. 5. Absorption and emission spectrum of POPOP.

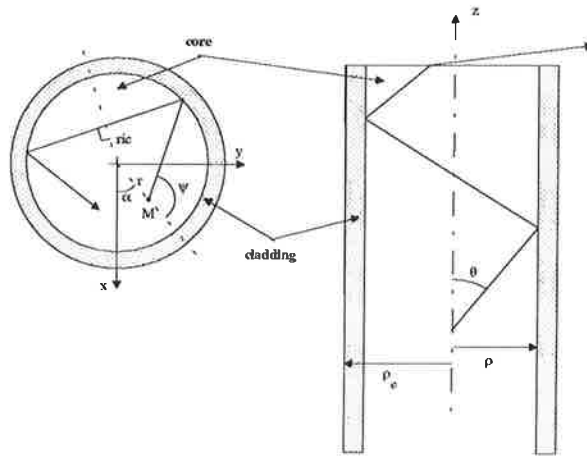


Fig. 6. Ray Parameters.

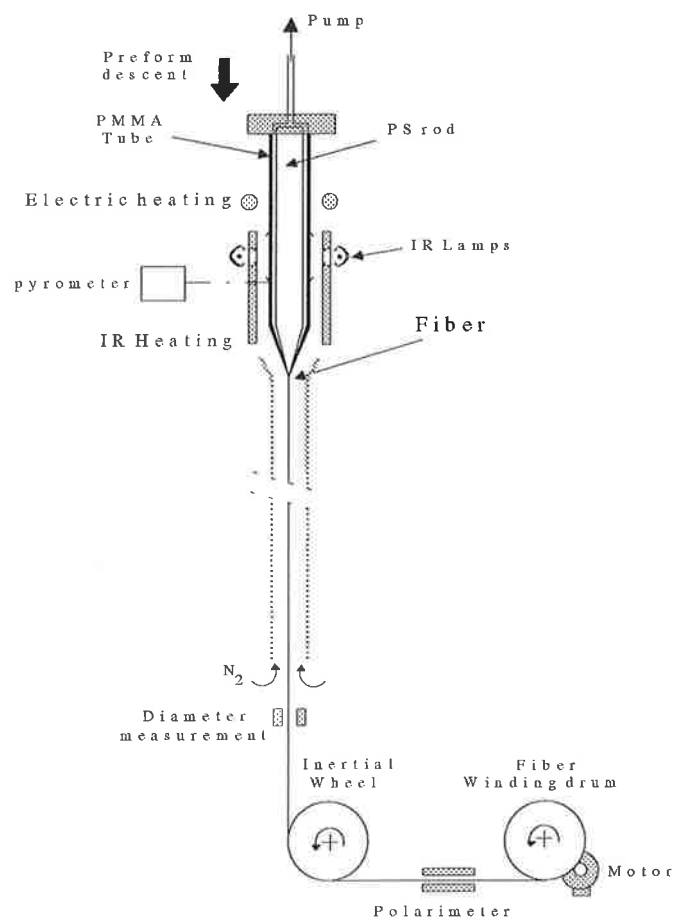


Fig. 7. Fiber pulling station.



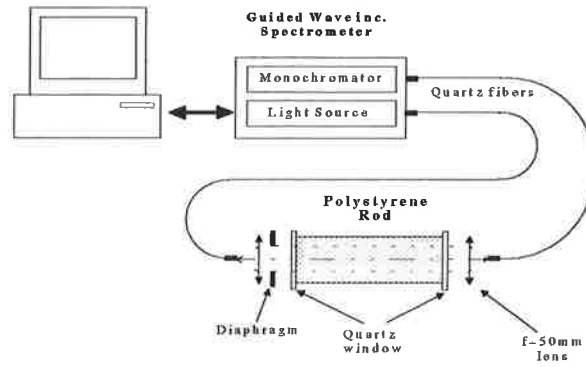


Fig. 8. Setup for the measurement of PS rods.

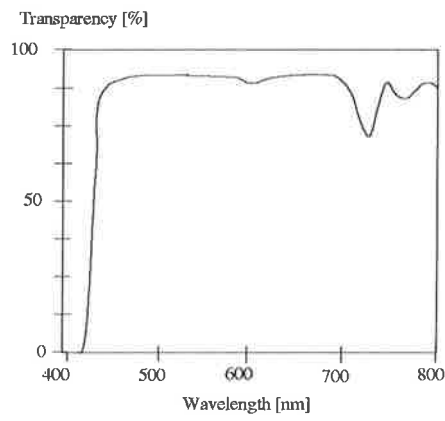


Fig. 9. Transmittance of a typical 400mm doped PS rod.

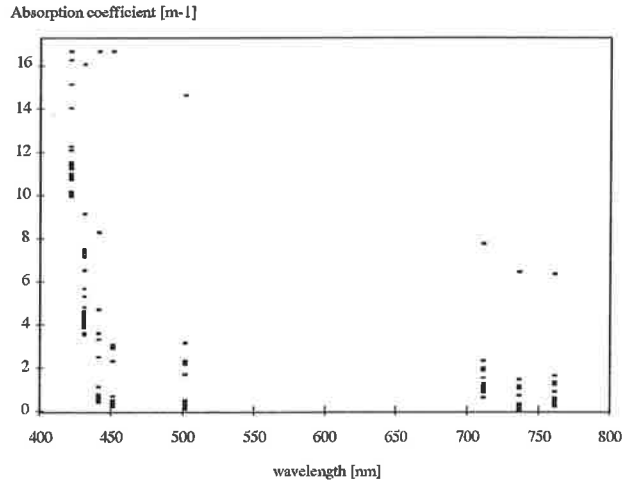


Fig. 10. Absorption coefficients measured in the various PS rods.

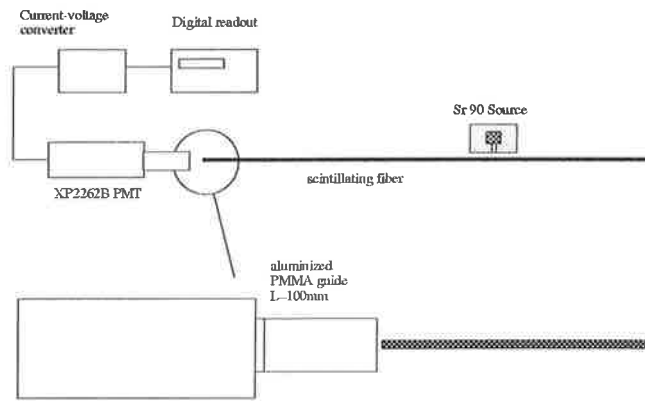


Fig. 11. Setup for the measurement of fiber light yield.

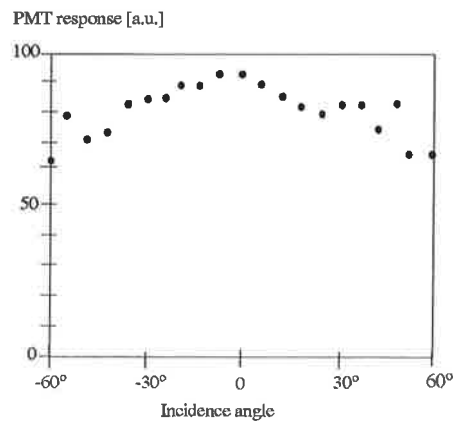


Fig. 12. Angular response of the PMT associated with the PMMA guide.

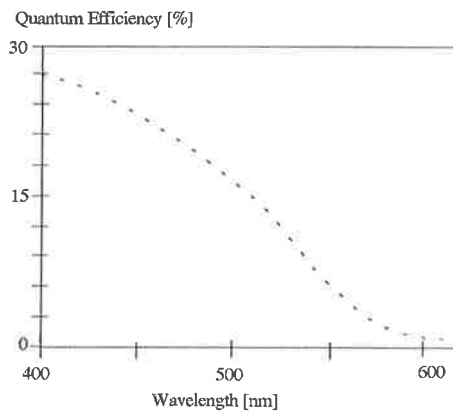


Fig. 13. Quantum efficiency of the PMT associated with the PMMA guide.

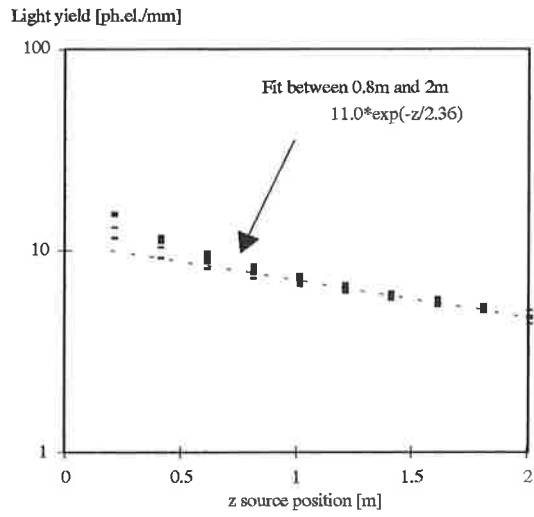


Fig. 14. Measurements of the fibers issued from the 4\_49\_0 preform.

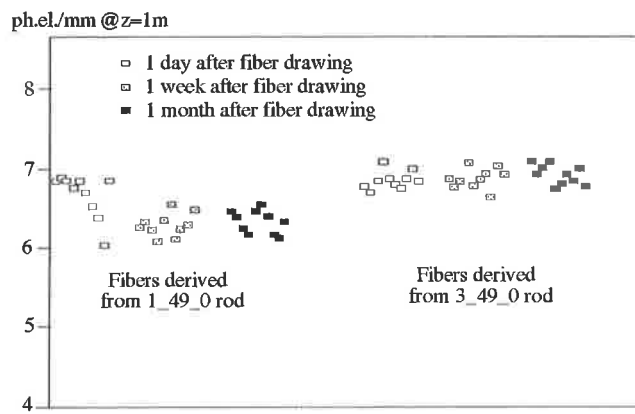


Fig. 15. Variation of the measurements after the drawing.

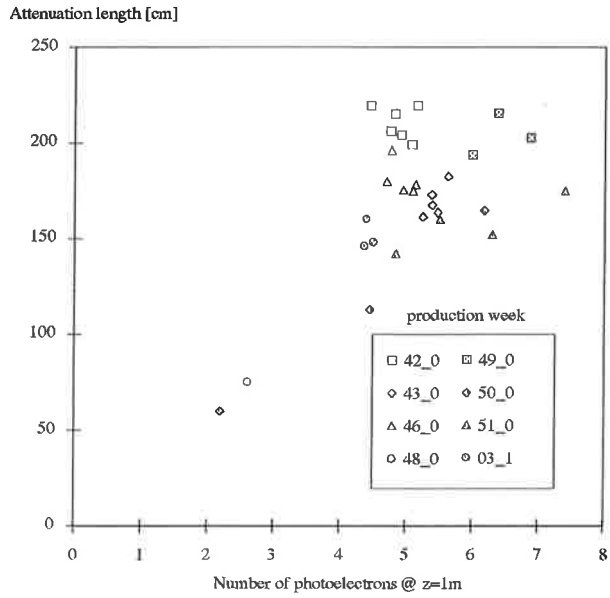


Fig. 16. Properties of scintillating fibers. Each point represents the mean values of 10 fibers.

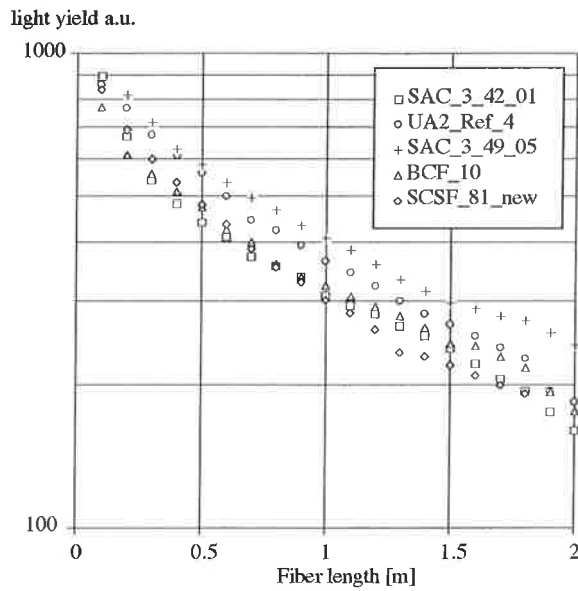


Fig. 17. Measurement of scintillating fibers from different manufacturers.

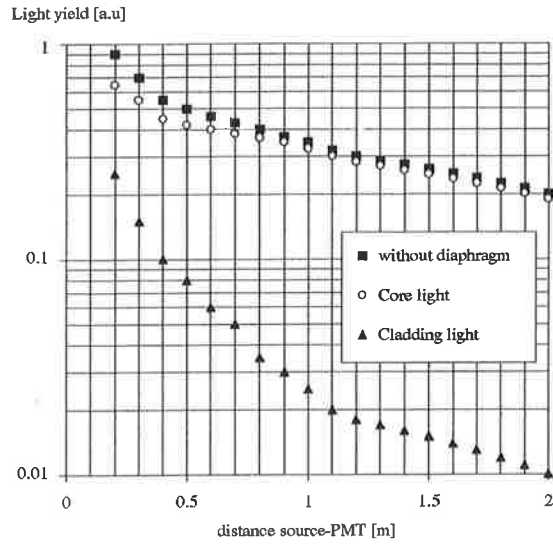


Fig. 18. Core and cladding light in a PS/PMMA scintillating fiber.

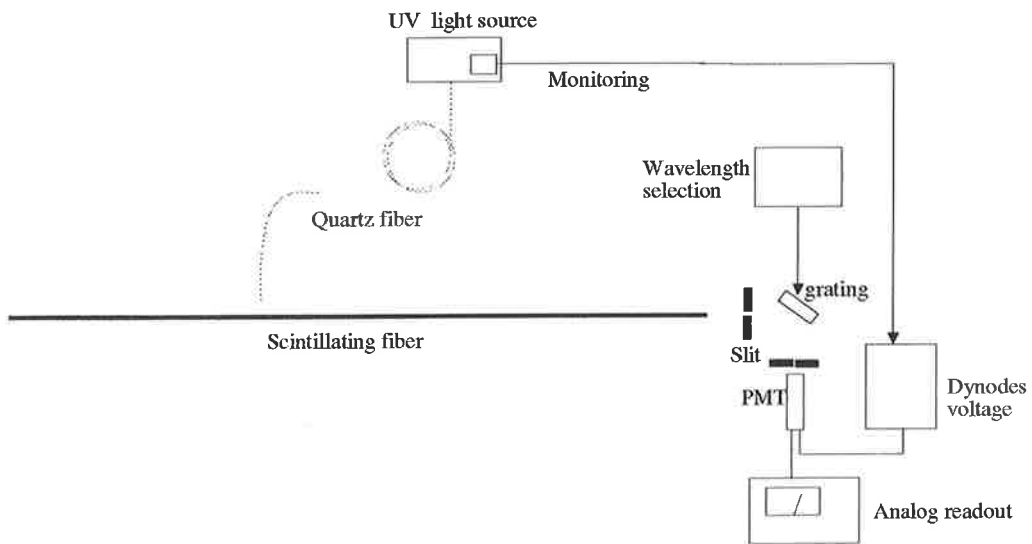


Fig. 19. Experimental setup for the measurement of fiber emission spectrum.

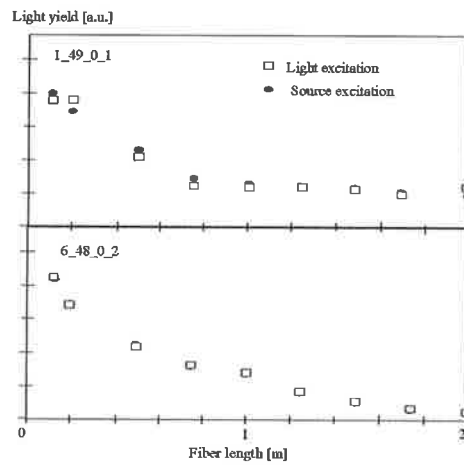


Fig. 20. Comparison of UV light and  $^{90}\text{Sr}$  source excitation

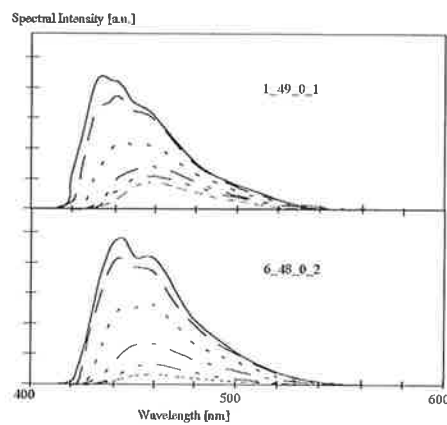


Fig. 21. Emission spectra as a function of fiber length for 1\_49\_01 and 6\_48\_02 fibers.  
 The spectra are measured at 0.1, 0.2, 0.5, 1, 1.5, 2 m.  
 The maximum of emission shifts from 440 nm to 460 nm.  
 After 0.5 m, the emission is almost stationary.

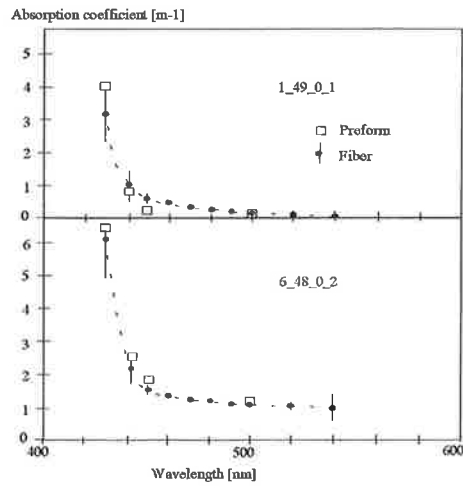


Fig. 22. Absorption of bulk material measured in scintillating fibers and in preform rods.

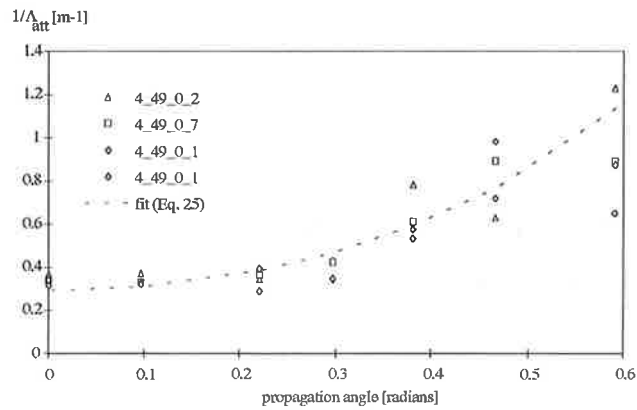


Fig. 23. Absorption measured in the PS/PMMA fibers derived from the 4\_49\_0 rod.

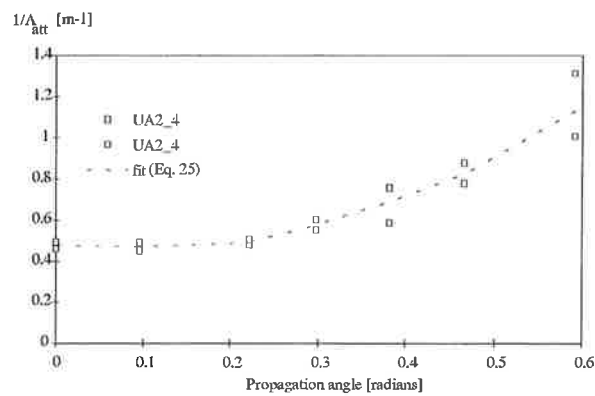


Fig. 24. Absorption measured in PS/PVA fibers.



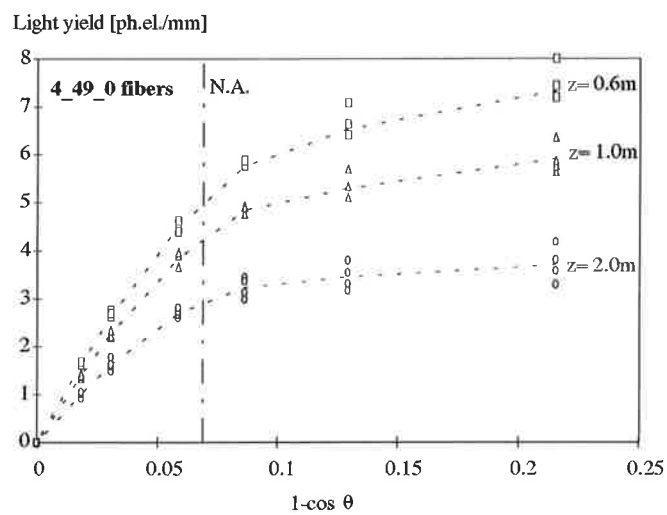


Fig. 25. Angular distribution of light in PS/PMMA fibers.

